

Superconductivity of two-dimensional hydrogenated transition-metal diborides.

Jakkapat Seeyangnok^{1,2}, Udomsilp Pinsook^{2*},
Graeme John Ackland^{1*}

¹Centre for Science at Extreme Conditions, School of Physics and Astronomy, University of Edinburgh, Edinburgh, United Kingdom.

²Department of Physics, Faculty of Science, Chulalongkorn University, Bangkok, Thailand.

*Corresponding author(s). E-mail(s): udomsilp.p@chula.ac.th;
gjackland@ed.ac.uk;
Contributing authors: jakkapatjtp@gmail.com;

Abstract

Since the discovery of MgB₂ with T_c=39K, various metal diborides of MB₂ have been intensively studied to find possible conventional high-temperature superconductors. A possible 2D structure of the metal diboride has been shown to be in the form of M₂B₂. Using density functional theory, we investigated phase stability and possible conventional superconductors for non-hydrogenation M₂B₂, light hydrogenation M₂B₂H, and heavy hydrogenation M₂B₂H₄ of transition metal borides M₂B₂ (M=Sc, Y, V, Nb). The light hydrogenation M₂B₂H show as if they were a perturbed system from the non-hydrogenation in which the electronic structure, the phonon property, and the possible superconducting state are slightly changed. However, the heavy hydrogenation of M₂B₂H₄ give very promising 2D materials with a possible high T_c of up to 84K at ambient pressure. This would fill the gaps for the study of possible conventional high-temperature superconductors at ambient pressure.

Keywords: Superconductivity, transition-metal borohydrides monolayer, and hydrogenated 2D materials.

1 INTRODUCTION

The discovery of superconducting MgB_2 [1] with $T_c=39\text{K}$ has ushered in a new era in the exploration of conventional high-temperature superconductors [2]. The composition of MB_2 metal diborides has received considerable attention due to the potential for high T_c at ambient pressure. Moreover, transition-metal diborides (MB_2) have been experimentally identified in NbB_2 [3], ZrB_2 [4], and TaB_2 [5]. These compounds possess a hexagonal crystal structure with $P6/mmm$ space-group symmetry. Following the successful fabrication of 2D MgB_2 (with $T_c=36\text{K}$ [6]), there has been a surge in research into 2D metal diborides. Recently, superconductivity in hexagonal layered transition metal diborides (MB_2) has been theoretically explored in [7], covering $M=\text{Sc, Zr, V, Nb, Ta, Cr, and Re}$ with T_c values of 20.4, 2.9, 8.3, 35.5, 7.1, 4.5, and 2.4 K, respectively. Additionally, investigations have extended to superconductivity in 2D metal borides MB_4 , including $M=\text{Be, Mg, Ca, Sc, and Al}$ with T_c values of 29.9, 22.2, 36.1, 10.4, and 30.9 K, respectively, as well as M_2B_2 , where $M=\text{Mg and Re}$ with T_c values of 3.2 and 5.5 K, respectively.

For bulk conventional high-temperature superconductors, attention has been primarily focused on bulk rich-hydrogen materials (hydrides) since the prediction of possible superconductivity in metallic hydrogen [8, 9]. Despite numerous successful theoretical predictions and experimental observations, such as the prediction of H_3S and LaH_{10} with $T_c \sim 200$ K [10] and $T_c \sim 280$ K [11, 12], and the corresponding experimental observations with $T_c \sim 203$ K at 150 GPa [13, 14] and $T_c \sim 250\text{-}260$ K at 170-180 GPa [15, 16], respectively, these hydrides require extremely high pressure for stabilization. For more practical applications, it is crucial to explore new forms of hydrides, especially those stable at ambient pressure. Recently, the bulk semiconductor $\text{Mg}(\text{BH}_4)_2$ hydride at ambient pressure has been demonstrated to exhibit metallic behavior with hole doping and a T_c up to 140 K [17]. Therefore, there is a growing interest in hydride forms stable at ambient pressure with potentially high T_c . Additionally, two-dimensional (2D) hydrides, particularly hydrogenated 2D materials, have undergone intensive investigation, showing promise for high superconducting temperatures.

There are two cases of 2D hydrides. First, elements in 2D materials are substituted with hydrogen atoms, such as Janus transitional-metal dichalcogenide hydrides (JTMDs), for incomplete list [18–22]. Second, 2D materials are hydrogenated without removing the original atoms from pristine 2D materials, as seen in doped hydrogenated graphene with a T_c above 90 K [23], Mo_2C_3 with a T_c of 53 K [24], and CuH_2 with a T_c greater than 40 K [25]. Moreover, hydrogenated MgB_2 was predicted to have a T_c of 67 K, which could increase to 100 K when applying 5% biaxial tensile strain [26], and hydrogenated phosphorus carbide, HPC_3 , was also predicted to exhibit a superconducting state with a T_c of approximately 31 K, increasing to 57.3 K when applying 3% biaxial tensile strain [27]. Recently, two-dimensional hydrogenated metal diborides, $\text{M}_2\text{B}_2\text{H}$ ($M=\text{Al, Mg, Mo, and W}$), have been predicted with T_c values of 52.64 K, 23.25 K, 21.54 K, and 18.67 K, respectively [28]. Furthermore, $\text{Ti}_2\text{B}_2\text{H}_4$ has been recently predicted to have a T_c of 48.6 K, which can be increased to 69.4 K with a tensile strain of 9% [29].

In this study, we systematically investigate 2D non-hydrogenated transition metal borides M_2B_2 ($M = \text{Sc}, \text{Y}, \text{V}, \text{and Nb}$), which have been suggested to exhibit dynamical and thermal stability in [30, 31], as well as light hydrogenated transition metal borides M_2B_2H and heavy hydrogenated transition metal borides $M_2B_2H_4$. We begin by discussing the lattice structure, stability, electronic structure, and potential conventional high-temperature superconductivity in heavy hydrogenated transition metal borides.

2 RESULTS AND DISCUSSIONS.

2.1 LATTICE STRUCTURE AND STABILITY.

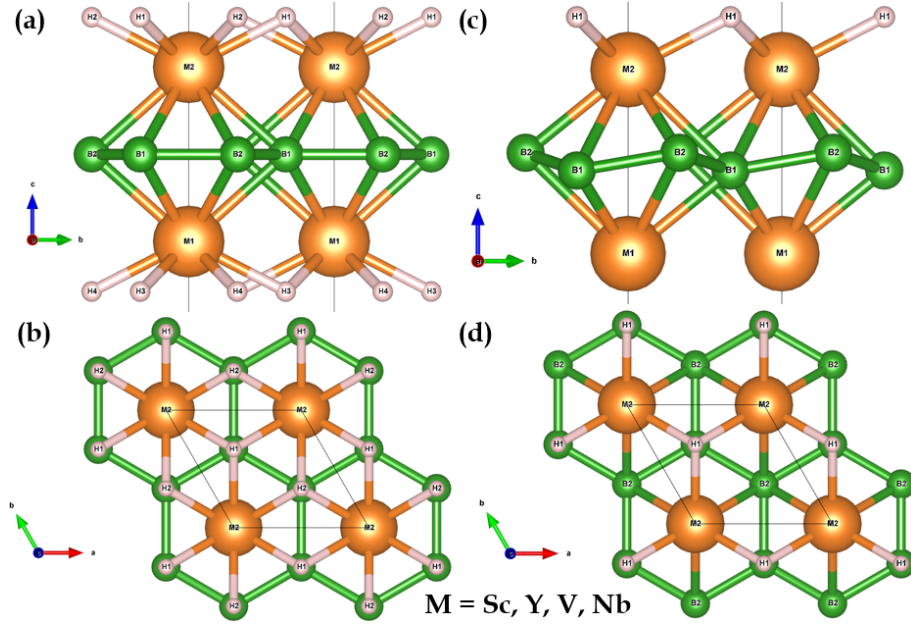


Fig. 1 (a) and (b) show side and top views of the 2D $M_2B_2H_4$ structure ($M = \text{Sc}, \text{Y}, \text{V}$ and Nb) where the transition metals (M), boron (B) and hydrogen (H) atoms are represented by orange, green and pink spheres, respectively. (c) and (d) show side and top views of the 2D M_2B_2H with the wrinkle of the boron layers.

The crystal structure of the $M_2B_2H_4$ monolayer is illustrated in Fig. 1. $M_2B_2H_4$ adopts a 3D hexagonal structure with a space group symmetry of $P6/mmm$, analogous to Mg_2B_2 . Fig. 1 presents the side view and top view of $M_2B_2H_x$ ($x=0,1,4$) in panels (a) and (b), respectively. In this structure, boron atoms (depicted as green spheres) form a honeycomb lattice at the Wyckoff positions $(1/3, 2/3)$ and $(2/3, 1/2)$, sandwiched between two layers of transition metals M (represented by orange spheres) at the top and bottom. Hydrogen atoms (shown as pink spheres) occupy the upper and lower layers, alongside transition metals, at the Wyckoff positions $(1/3, 2/3)$ and $(2/3, 1/2)$.

The optimized lattice parameters of $M_2B_2H_4$, M_2B_2H , and M_2B_2 are summarized in Table 1. The lattice constants of $M_2B_2H_4$ and M_2B_2H ($M = \text{Sc}, \text{Y}, \text{V}, \text{and Nb}$) are 3.18, 3.41, 2.93, and 3.06 Å, and 3.13, 3.32, 2.94, and 3.10 Å, respectively. For M_2B_2 , the lattice constants are 3.12, 3.29, 2.94, and 3.10 Å, respectively. In the case of light hydrogenated configurations, a hydrogen atom (H1) induces wrinkles in the honeycomb boron monolayer, as depicted in panels (c) and (d) of Figure 1. The extent of wrinkling is quantified by the perpendicular distance between the two layers of wrinkled boron atoms, denoted as δB (B2:B1), and is measured as $\delta B = 2.80, 3.04, 2.43,$ and 2.62 Å, respectively. The distances between the two transition metal layers (M2:M1) for $M_2B_2H_4$ and M_2B_2H are 3.60, 3.92, 2.96, 3.32 Å, and 3.46, 3.74, 2.83, 3.06 Å, respectively.

For the non-hydrogenated case, the distances between M2 and M1 are 3.46, 3.76, 2.80, and 3.04 Å. The distances between the transition metals and the middle honeycomb layer of boron (M2:B1) are 1.80, 1.96, 1.48, and 1.66 Å. In the case of non-hydrogenated and light hydrogenated configurations, these distances are 1.75, 3.12, 3.29, 2.94, and 3.10 Å, respectively. For M_2B_2 , the distances between M2 and B1 are 3.12, 3.29, 2.94, and 3.10 Å, respectively. Furthermore, in addition to $M_2B_2H_4$ and M_2B_2H , the distances between the hydrogen atom layer and the boron layer (H1:B1) are 2.58, 2.78, 2.46, and 2.74 Å for heavy hydrogenated and light hydrogenated cases, respectively.

2D materials	a (Å)	M2:M1 (Å)	M2:B1 (Å)	δB (Å)	H1:B1 (Å)	ΔH (eV)
Sc ₂ B ₂	3.12	3.46	1.73	-	-	-22.9
Y ₂ B ₂	3.29	3.76	1.88	-	-	-22.3
V ₂ B ₂	2.94	2.80	1.40	-	-	-28.7
Nb ₂ B ₂	3.10	3.04	1.52	-	-	-31.5
Sc ₂ B ₂ H	3.13	3.46	1.75	0.040	2.80	-26.7
Y ₂ B ₂ H	3.32	3.74	1.87	0.018	3.04	-26.6
V ₂ B ₂ H	2.94	2.83	1.46	0.021	2.43	-32.7
Nb ₂ B ₂ H	3.10	3.06	1.56	0.003	2.62	-35.7
Sc ₂ B ₂ H ₄	3.18	3.60	1.80	-	2.58	-38.5
Y ₂ B ₂ H ₄	3.41	3.92	1.96	-	2.78	-37.9
V ₂ B ₂ H ₄	2.93	2.96	1.48	-	2.46	-43.1
Nb ₂ B ₂ H ₄	3.06	3.32	1.66	-	2.74	-46.0

Table 1 The table shows the lattice constants, distances between the two transition metal layers (M2:M1), distances between the transition metals and the middle honeycomb layer of boron (M2:B1), the distance between the two layers of wrinkled boron atoms δB (B2:B1), the distances between the hydrogen atom layer and the boron layer (H1:B1), and the formation energy, respectively.

The stability of these $M_2B_2H_4$, M_2B_2H and M_2B_2 are explored systematically. The phonon dispersion of M_2B_2 , as shown in Figure 4, along the common high-symmetry path shows dynamical stable lattice dynamics. Furthermore, it has also recently been investigated in [30, 31] that Sc₂B₂, Y₂B₂, V₂B₂, and Nb₂B₂ are dynamically and thermally stable. Similarly, $M_2B_2H_4$ and M_2B_2H also show non-negative frequency in phonon dispersion, as shown in Fig. 4. A detailed discussion of the phonon spectrum will be discussed later. In addition, we can also examine the energy associated with the formation of a crystal structure from its constituent elements, the formation energy

given by

$$E_{\text{formation}} = E_{\text{structure}} - 2E_{\text{M}} - 2E_{\text{B}} - 4E_{\text{H}}, \quad (1)$$

$$E_{\text{formation}} = E_{\text{structure}} - 2E_{\text{M}} - 2E_{\text{B}} - E_{\text{H}}, \quad (2)$$

and

$$E_{\text{formation}} = E_{\text{structure}} - 2E_{\text{M}} - 2E_{\text{B}}, \quad (3)$$

for $\text{M}_2\text{B}_2\text{H}_4$, $\text{M}_2\text{B}_2\text{H}$ and M_2B_2 , respectively where E_{M} , E_{B} and E_{H} are isolated transition metals, boron and hydrogen atom, respectively. The formation energies of $\text{M}_2\text{B}_2\text{H}_4$ and $\text{M}_2\text{B}_2\text{H}$ are -38.5, -37.9, -43.1 and -46.0eV, and -26.7, -26.6, -32.7 and -35.7eV, respectively. These formation energies of 2D $\text{M}_2\text{B}_2\text{H}_4$ and $\text{M}_2\text{B}_2\text{H}$ are even smaller than those of M_2B_2 where formation energies of M_2B_2 are -22.9, -22.3, -28.7, -31.5eV, respectively. These results show that the 2D $\text{M}_2\text{B}_2\text{H}_4$ and $\text{M}_2\text{B}_2\text{H}$ are thermodynamic feasibility and are possible to synthesize under appropriate experimental conditions.

2.2 ELECTRONIC STRUCTURE.

To systematically study the electronic properties of the 2D $\text{M}_2\text{B}_2\text{H}_4$, $\text{M}_2\text{B}_2\text{H}$ and M_2B_2 , we will investigate the electronic structures presented in Figure 2. In general, $\text{M}_2\text{B}_2\text{H}_4$, $\text{M}_2\text{B}_2\text{H}$ and M_2B_2 show metallic behavior as a result of crossing electronic bands at the Fermi level. These crossing bands are generally dominated by the transition metal d-orbital electrons, which can be grouped into $A'(d_{z^2})$, $E'(d_{xy}, d_{x^2-y^2})$ and $E''(d_{yz}, d_{xz})$ at the Γ point.

From Figure 2 showing the orbital-resolved electronic band structure, the electronic density of states (EDOS) and the orbital projected density of states (PDOS), it is clear that all pristine M_2B_2 (M=Sc,Y,V,NB) are a metal having d-orbital dominated bands crossing the Fermi level. For III-TM group (Sc,Y), Sc_2B_2 and Y_2B_2 have the similar electronic band structure, which is dominated by d-orbital electrons of d_{z^2} , d_{xy} , $d_{x^2-y^2}$ and d_{yz} , d_{xz} . For Sc_2B_2 , we have three bands along the Γ point to K , a single band along the K point to the M point, and an intersection of a single u-shaped band along the M point to the Γ point crossing the Fermi level. The intersection forms the pocket of the Fermi surface, as shown in Figure 3. This also occurs for Y_2B_2 which results in the same Fermi surface topology between Sc_2B_2 and Y_2B_2 . With the light hydrogenation $\text{M}_2\text{B}_2\text{H}$, the electronic structures are slightly modified by the additional hydrogen atom that bonds to the TM (Sc and Y). As a result, we have several Fermi surface pockets that break into a single connected Fermi surface, as shown in Figure 3 of $\text{Sc}_2\text{B}_2\text{H}$ and $\text{Y}_2\text{B}_2\text{H}$. The electronic density of states remains almost unchanged. This indicates that the addition of a hydrogen atom slightly perturbs the electronic bands because of the small overlap between the wavefunction of the pristine system and the hydrogen atom. For the heavy hydrogenation of $\text{Sc}_2\text{B}_2\text{H}_4$ and $\text{Y}_2\text{B}_2\text{H}_4$, we have almost new electronic structures and electronic density of states, as shown in Figure 2. The electronic density of states at the Fermi level decreases significantly as a result of the bonding of d-orbital electrons with additional hydrogenation. For $\text{Y}_2\text{B}_2\text{H}_4$, d orbital no longer totally dominates, in which the PDOS of the p_x , p_y , p_z orbitals of the boron atom and the s orbital of the hydrogen atom become comparable with d-orbital electrons from Y atoms. On the other hand, for $\text{Sc}_2\text{B}_2\text{H}_4$ d orbital still

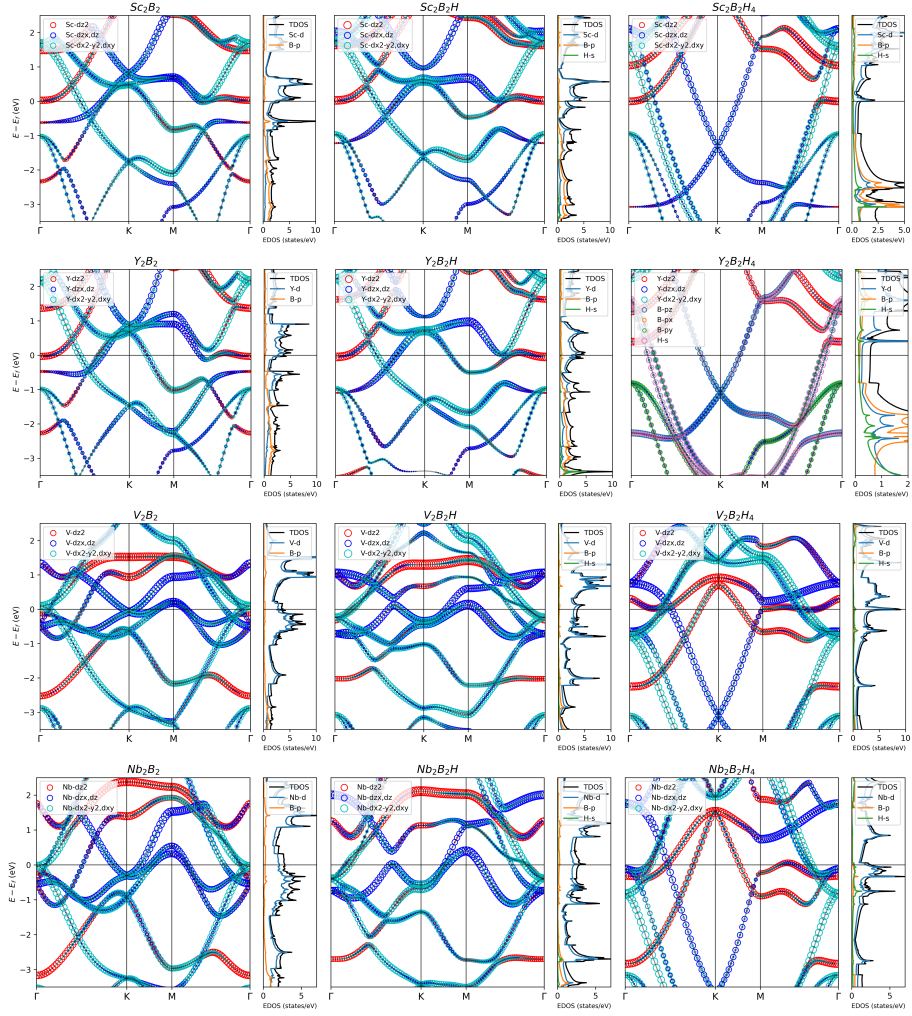


Fig. 2 The electronic structures of the 2D $M_2B_2H_4$, M_2B_2H , and M_2B_2 show the orbital-resolved band structure, projected electronic density of states for d-orbital of TM (Sc,Y,V,Nb), p-orbital of boron atom, and s-orbital of hydrogen atom.

dominate at Fermi level, and near the Γ point there are flat bands close to the Γ point which results in a high electronic density of states of van Hove singularity (vHs).

For V-TM (V, Nb) group, we have the same scenario as in the case of the III-TM group (Sc, Y) where the electronic bands and the electronic density of the state of V_2B_2H and Nb_2B_2H are slightly perturbed by an additional single hydrogen atom to the pristine compounds of V_2B_2 and Nb_2B_2 . The pristine V_2B_2 have a small Fermi surface pocket, as shown in Figure 3, near the Γ point along the Γ point to the K point due to the crossing of the upper and lower bands, as shown in Figure 2. An additional hydrogen atom slightly changes the electronic structure of V_2B_2 by removing these pockets with two shells of smooth connected Fermi surfaces near the

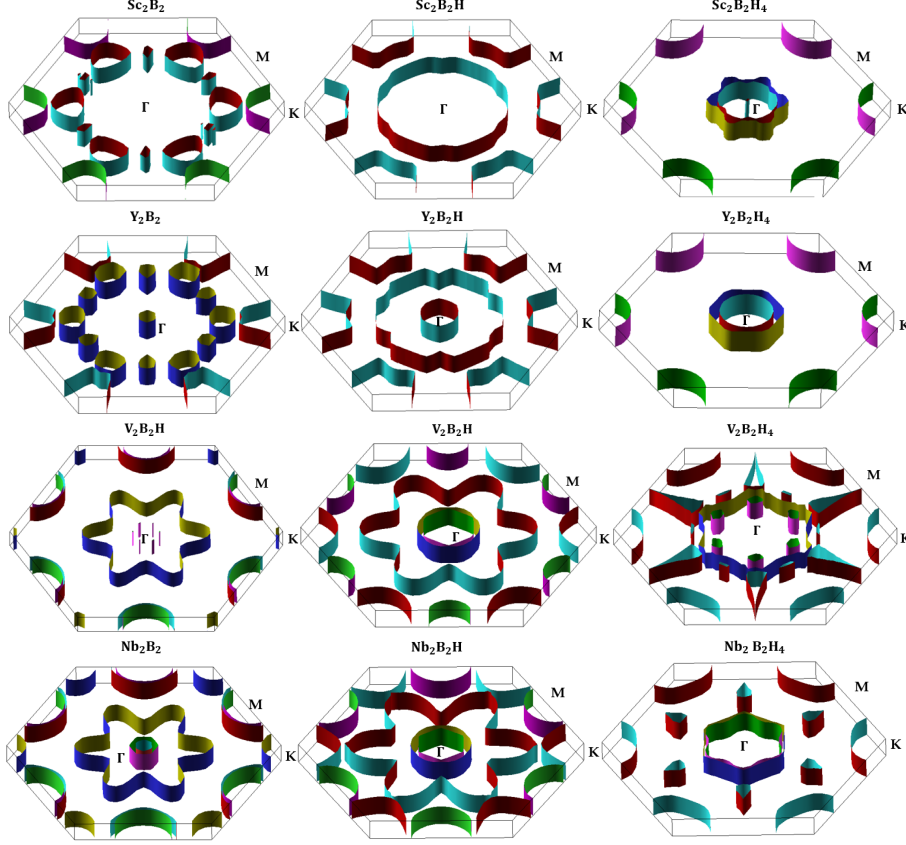


Fig. 3 These figures show the Fermi surfaces of the 2D heavy hydrogenated $M_2B_2H_4$, light hydrogenated M_2B_2H , and non-hydrogenated M_2B_2 where $M=Sc, Y, V, Nb$.

Γ point. For Nb_2B_2H , the electronic d-orbital dominated bands slightly shift due to the perturbation of hydrogenation, but the topology of the Fermi surface remains unchanged compared to the pristine Nb_2B_2 , except that the open two-shell Fermi surfaces around the M point become a single opened Fermi surface due to the lack of a crossing band along the M point to Γ , as shown in Figure 3. For heavy hydrogenation, we have the special characteristics of an electronic band at the Fermi level along the Γ point to the M point that shows a flat dispersion close to the M point along the Γ point to the M point, and near the Γ point along the Γ point to the M point resulting in a high electronic density of states of van Hove singularity (vHs) at the Fermi level, as shown in Figure 2 of $V_2B_2H_4$. For $Nb_2B_2H_4$, even though we also have peaks of vHs, the Fermi level is not at any of these vHs. Therefore, this main difference between the V-TM (V, Nb) and III-TM (Sc, Y) groups is that the electronic density of the states of the III-TM (Sc, Y) group decreases significantly from non- and light hydrogenation to heavy hydrogenation, which is opposite to the V-TM group. Therefore, we would expect that the V-TM group would favor electron-phonon coupling, which we shall discuss later. These results suggest that the disrupted evolution of the electronic band

topology of Fermi surfaces can be slightly changed and heavily disrupted due to the amount of extra composition elements.

2.3 Phonon Properties

As shown in Figure 4, the phonon spectrum of hydrogenated transition metal borides of $M_2B_2H_4$, M_2B_2H and M_2B_2 show dynamically stable lattice dynamics by having non-negative spectrum in phonon dispersion and phonon density of states.

For the III-TM group, we have a similar phonon dispersion between Sc_2B_2 and Y_2B_2 , except that the phonon spectrum in general for Y_2B_2 is suppressed to a lower energy because of a larger mass of yttrium. Mode 9 (out-of-plane boron vibration) of Y_2B_2 also becomes a higher energy mode than mode 10 (out-of-plane boron vibration) compared to Sc_2B_2 as shown in Table 2 for eigenvalues at the Γ point where the eigenvectors for each modes of M_2B_2 are shown in (a) of Figure 5. For the III-TM group, we have three acoustic modes, namely a longitudinal in-plane acoustic mode (LA), a transverse acoustic in-plane mode (TA), and a flexural out-of-plane acoustic mode (ZA) that ranges from higher to lower energy, respectively, as shown in Figure 4 when moving away from the Γ point. The nine optical modes correspond to the vibration of the transition-metal and boron atoms, as shown in Figure 5. The transition-metal vibrations consist of two degenerate in-plane vibrations (modes 4,5), and an out-of-plane vibration (mode 6). The other four non-degenerate optical modes of boron vibrations result from two degenerate in-plane vibrations (modes 7,8), two degenerate in-plane vibrations (modes 11,12), an and out-of-plane vibrations (modes 9, 10, respectively), as shown in Figure 5. Similarly to the III-TM group, the phonon spectrum of the V-TM group namely, V_2B_2 and Nb_2B_2 , share a common phonon dispersion and phonon density of states, except that the phonon dispersion in Nb_2B_2 have a lower energy due to a larger mass of niobium (almost twice that of vanadium). The out-of-plane boron vibration (mode 9) also gets lower energy, and in-plane mode (mode 7,8) then becomes higher than mode 9. The energy eigenvalues and eigenvectors of the normal optical modes of M_2B_2 is summarized in Table 2, and shown in Figure 5.

Modes (Eigenvectors)	$\omega(Sc_2B_2)$ meV	$\omega(Y_2B_2)$ meV	$\omega(V_2B_2)$ meV	$\omega(Nb_2B_2)$ meV
4,5 (IP)	23.76	15.72	31.31	22.21
6 (OP)	31.33	21.45	38.24	28.94
7,8 (IP)	47.32	41.64	66.76	62.65
9 (OP)	55.89	65.77	65.54	69.11
10 (OP)	67.62	50.86	70.48	69.65
11,12 (IP)	100.21	81.67	116.89	92.87

Table 2 For the first column, it shows the eigenvectors of M_2B_2 (M=Sc,Y,V,Nb) where the direction of vibration referred as out-of-plane (OP) or in-plane (IP), and the type of atom vibrations respectively. The visualization of these eigenvectors is shown in Figure 5. The other columns show the corresponding eigenvalues for each vibration modes.

When hydrogenating a single hydrogen atom in the cases of Sc_2B_2H and Y_2B_2H , we have perturbed systems in which the perturbation slightly changes the original system and the vibrations of hydrogen atoms are also coupled with transition-metal atoms and boron. However, we still have the same eigenvectors of M_2B_2 that couples

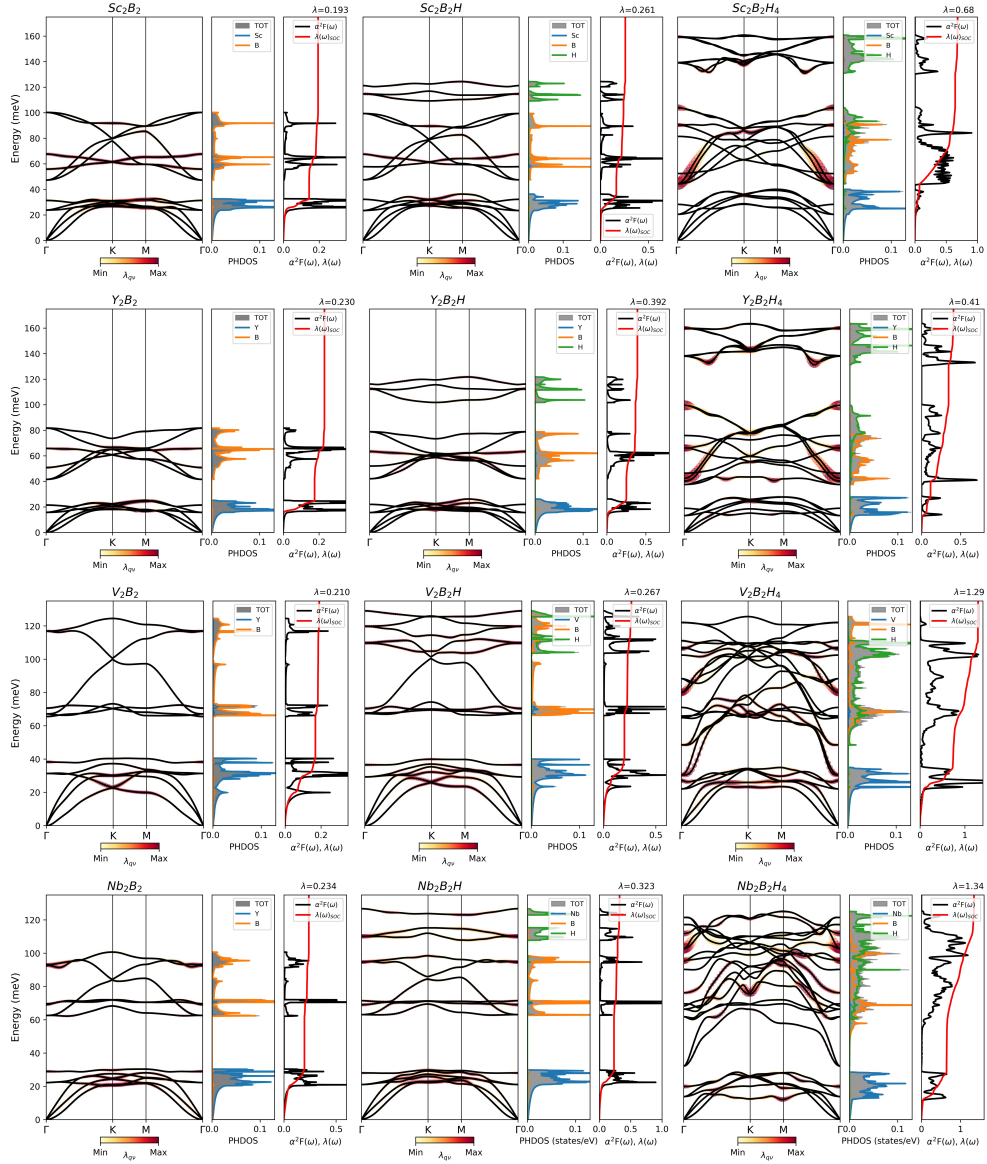


Fig. 4 These plots show the weighted electron-phonon coupling (EPC) dispersion of the phonon, the projected phonon density of the states (PHDOS), the isotropic Eliashberg spectral function $\alpha^2 F(\omega)$ and the spectrum-dependent electron-phonon coupling $\lambda(\omega)$ of 2D $M_2B_2H_4$, M_2B_2H , and M_2B_2 .

the vibrations of hydrogen atoms as shown in (b) of Figure 5 with three additional optical modes (mode 13,14,15). These three optical phonon spectrum results primarily from two degenerate in-plane boron-coupled hydrogen vibrations (mode 13,14), and an out-of-plane boron-coupled hydrogen vibration (mode 15) as the highest energy optical

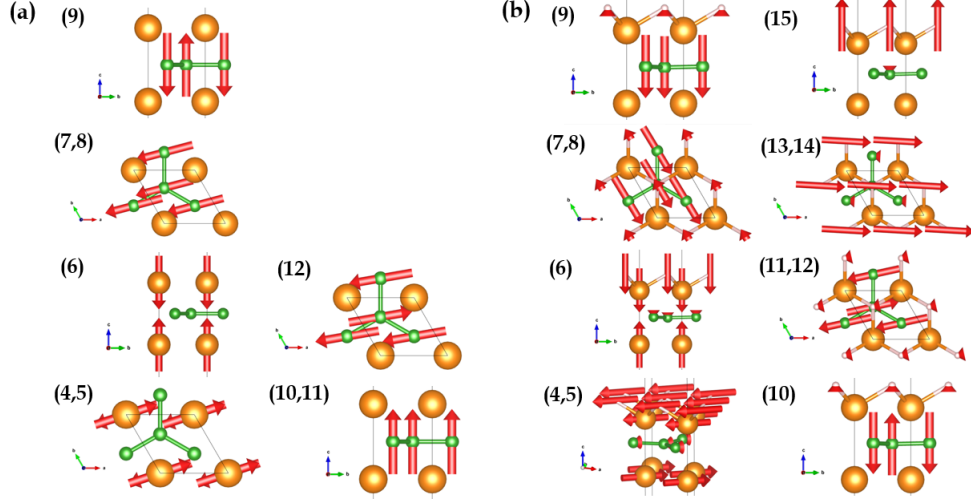


Fig. 5 (a) shows the normal vibration modes of M_2B_2 , and (b) shows the normal vibration modes of M_2B_2H ($M=Sc, Y, V, Nb$)

phonon mode in M_2B_2H . The three extra optical modes of a hydrogen atom vibration give the highest energy spectrum, obviously separated from the other nice optical modes. For Nb_2B_2H , the situation is similar for the eigenvectors and eigenvalues to that of the III-TM group, as given in Table 3. However, the spectrum of in-plane hydrogen-coupled boron vibrations (mode 11,12) becomes higher than in-plane boron-coupled hydrogen vibrations (mode 13,14). This is why the contribution of boron vibrations becomes significant in the highest energy spectrum of V_2B_2H as shown in the projected phonon density of states Figure 4. The energy eigenvalues and eigenvectors of the normal optical modes of M_2B_2H is summarized in Table 3, and shown in Figure 5.

Modes (Eigenvectors)	$\omega(Sc_2B_2H)$ meV	$\omega(Y_2B_2H)$ meV	$\omega(V_2B_2H)$ meV	$\omega(Nb_2B_2H)$ meV
4,5 (IP)	23.40	15.62	29.79	19.62
6 (OP)	32.19	21.97	36.62	27.35
7,8 (IP)	47.41	42.06	67.38	62.75
9 (OP)	57.82	52.00	70.33	69.56
10 (OP)	67.62	63.37	67.74	71.98
11,12 (IP)	99.32	78.79	119.77	94.43
13,14 (IP)	114.68	112.41	109.80	110.05
15 (IP)	121.18	116.16	128.99	126.70

Table 3 For the first column, it shows the eigenvectors of M_2B_2H ($M=Sc, Y, V, Nb$) where the direction of vibration referred as out-of-plane (OP) or in-plane (IP), and the type of coupled-atom (X) atom (Y) vibrations (XY), respectively. The visualization of these eigenvectors is shown in Figure 5. The other columns show the corresponding eigenvalues for each vibration modes.

For heavy hydrogenation, the addition of four additional hydrogen atoms completely modify the phonon dispersion of non-hydrogenated cases. For the heavy

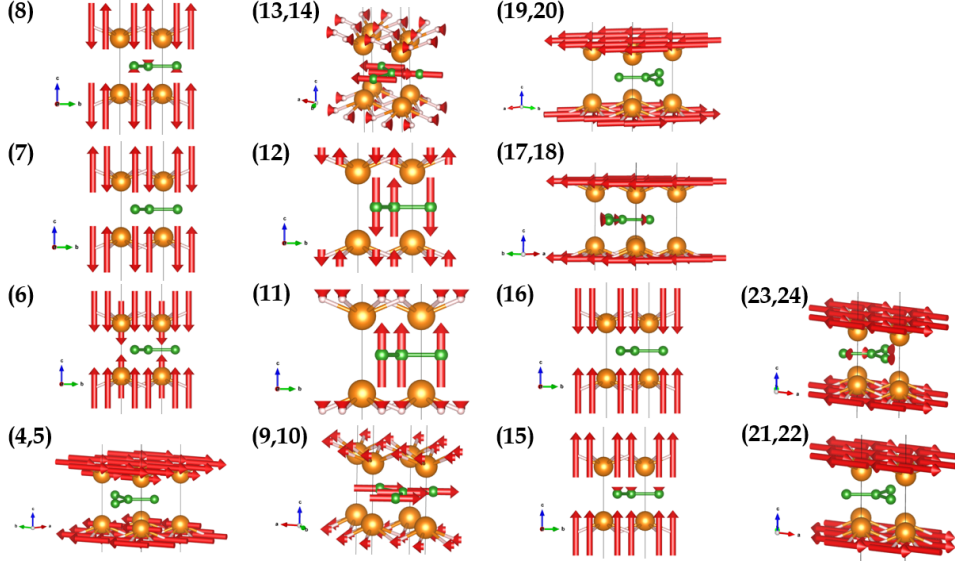


Fig. 6 shows the normal vibration modes $M_2B_2H_4$ ($M=Sc, Y, V, Nb$).

Modes (Eigenvectors)	$\omega(Sc_2B_2H_4)$ meV	$\omega(Y_2B_2H_4)$ meV	$\omega(V_2B_2H_4)$ meV	$\omega(Nb_2B_2H_4)$ meV
4,5 (IP)	20.48	13.25	23.31	12.34
6 (OP)	28.21	18.97	28.00	21.34
7 (OP)	44.37	40.28	102.43	76.17
8 (OP)	44.40	42.47	107.11	90.22
9,10 (IP)	44.59	37.52	64.92	61.84
11 (OP)	52.44	46.41	65.93	68.38
12 (OP)	81.51	75.88	70.99	69.60
13,14 (IP)	90.42	66.13	122.03	95.46
15 (OP)	103.75	99.61	111.07	117.15
16 (OP)	104.08	99.51	106.17	111.80
17,18 (IP)	139.02	138.00	30.86	32.21
19,20 (IP)	139.31	138.32	48.78	32.22
21,22 (IP)	159.29	159.81	88.43	121.46
23,24 (IP)	159.43	160.04	80.10	102.73

Table 4 For the first column, it shows the eigenvectors of $M_2B_2H_4$ ($M=Sc, Y, V, Nb$) where the direction of vibration referred as out-of-plane (OP) or in-plane (IP), and the type of coupled-atom (X) atom (Y) vibrations (XY), respectively. The visualization of these eigenvectors is shown in Figure 6. The other columns show the corresponding eigenvalues for each vibration modes.

hydrogenation of $Sc_2B_2H_4$, the phonon of in-plane vibrations from boron-coupled hydrogen vibrations and hydrogen vibrations dominates the spectrum at 140 and 160meV. Phonon at 140meV results from two degenerate in-plane boron-coupled hydrogen vibrations (modes 17,18) and two degenerate in-plane hydrogen vibrations (mode 19,20). The phonon at 160meV results from two degenerate in-plane hydrogen

vibrations (mode 21,22) and two degenerate in-plane boron-coupled hydrogen vibrations (mode 23,24). This forms the first group of phonon spectrum at the highest energy. The second group of the phonon spectrum in the moderate energy range of $\text{Sc}_2\text{B}_2\text{H}_4$ results from eight eigenvalues of about 40meV to 100meV. It consists of out-of-plane hydrogen vibration (mode 7), out-of-plane boron-coupled hydrogen (mode 8), two degenerate in-plane hydrogen-coupled boron vibrations (mode 9,10), out-of-plane hydrogen-coupled boron vibration (mode 11), out-of-plane hydrogen-coupled boron vibration (mode 12), two degenerate in-plane hydrogen-coupled boron vibrations (mode 13,14), out-of-plane boron-coupled hydrogen vibration (mode 15), and out-of-plane hydrogen vibration (mode 16), as shown in Figure 6. In the lowest group of phonon spectrum, we have three acoustic modes, two degenerate in-plane transition-metal atom vibrations (mode 4,5), and an out-of-plane transition-metal atom vibration (mode 6). This forms the phonon spectrum at low energy. For $\text{Y}_2\text{B}_2\text{H}_4$, even though we have the shift up and down of energy eigenvalues as shown in Table 4. However, these shifts still occur in the same range for each group of the phonon spectrum as previously discussed for $\text{Sc}_2\text{B}_2\text{H}_4$. As a result, the phonon spectrum of $\text{Sc}_2\text{B}_2\text{H}_4$ and $\text{Y}_2\text{B}_2\text{H}_4$ is occupied three regions of energies, as shown in Figure 4.

For the V-TM group, the phonon dispersion is also completely modified by hydrogenation, similar to that for the group III-TM. The main difference is that the phonon spectrum of hydrogen and boron-coupled hydrogen vibrations have lower energies. On the other hand, the phonon spectrum of hydrogen-coupled boron vibrations has a higher energy, as summarized in Table 4 for the detailed shift of each eigenvalue of the vibration. Therefore, the phonon spectrum of $\text{V}_2\text{B}_2\text{H}_4$ and $\text{Nb}_2\text{B}_2\text{H}_4$ is occupied two regions of energies, as shown in Figure 4. In the case of $\text{V}_2\text{B}_2\text{H}_4$, the highest phonon energy no longer results from hydrogen vibration (mode 21,22 for $\text{Nb}_2\text{B}_2\text{H}_4$) or boron-coupled hydrogen vibration (mode 23,24 for $\text{Sc}_2\text{B}_2\text{H}_4$ and $\text{Y}_2\text{B}_2\text{H}_4$) as shown in Table 4, rather than two degenerate hydrogen-coupled boron vibrations (Mode 12,13). This is the reason why we have boron as the main contribution to the phonon spectrum, as shown in the projected phonon density of the states of $\text{V}_2\text{B}_2\text{H}_4$ of Figure 4.

2.4 Electron-Phonon coupling and phonon-mediated superconductivity.

The electron-phonon coupling (EPC) is investigated via the weighted EPC dispersion of the phonon and the contour plot of EPC (λ_{qv}) as shown in Fig. 4 and Fig. 7, respectively. In general, the EPC primarily arises near the Γ point for $\text{Sc}_2\text{B}_2\text{H}_4$, $\text{V}_2\text{B}_2\text{H}_4$, and $\text{Nb}_2\text{B}_2\text{H}_4$. For $\text{Sc}_2\text{B}_2\text{H}_4$, this contribution comes from the optical vibration modes $\nu = 7 - 10$, specifically the out-of-plane hydrogen vibrations ($\nu = 7, 8$) and the out-of-plane boron vibrations ($\nu = 9, 10$). For $\text{V}_2\text{B}_2\text{H}_4$, the EPC is largely contributed near the Γ point ($\nu = 6 - 8, 15 - 16$), but it also results from various vibration modes away from the Γ point. This behavior is observed in the weighted EPC dispersion of the phonon in the energy range around 70 meV between the K point and the M point, as shown in Fig. 4. This leads to a high average electron-phonon coupling function of the Eliashberg function, with significant contributions around 30 meV, 70 meV, and 100 meV, resulting in a large λ value of 1.29. For $\text{Nb}_2\text{B}_2\text{H}_4$, the Eliashberg function is divided into two regions: lower energy and higher energy. The EPC at lower energy,

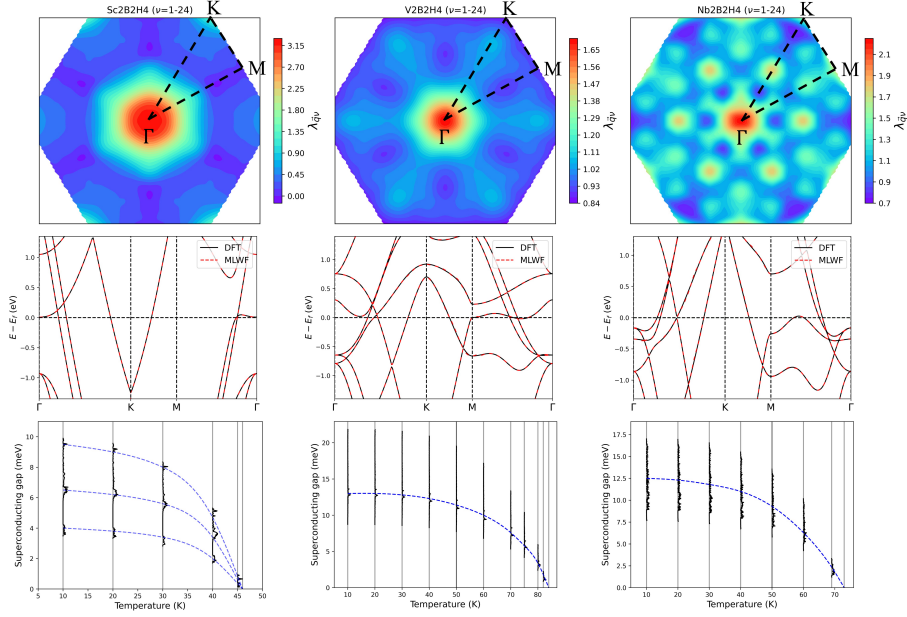


Fig. 7 The three-upper images show the electron-phonon coupling distributed over the Brillouin zone, the three-lower middle images show the comparison between the electronic bands obtained from DFT and maximally-localised Wannier function, and the three-lower images show the superconducting gap of $\text{Sc}_2\text{B}_2\text{H}_4$, $\text{V}_2\text{B}_2\text{H}_4$, and $\text{Nb}_2\text{B}_2\text{H}_4$, respectively.

around 20 meV, results from the phonon excitation of niobium away from the Γ point. At higher energy, the EPC is distributed throughout the Brillouin zone for the optical vibrations of boron and hydrogen. Consequently, the net contour map of EPC shows peaks of λ_{qv} throughout the Brillouin zone, leading to the highest value of λ .

According to Eq.(??), the Eliashberg spectral function depends on the product of the transition matrix, the Fermi nesting function, and the phonon spectrum. To obtain a high superconducting temperature (T_c), we need large values of electron-phonon coupling (λ), and a high logarithmic average of the phonon spectrum ω_{\log} . Important values to determine the superconducting temperature are shown in Table 5 together with other possible superconductors that have previously been studied. For non-hydrogenated M_2B_2 , they are not superconductors (or millikelvin scale superconductors, which we neglect here), and light hydrogenation barely changes their superconducting properties. For the III-TM group, we notice only minor changes in both λ and ω_{\log} that are $\Delta\lambda=0.068$ and $\Delta\omega_{\log}=5.1\text{meV}$ for light hydrogenation of Sc_2B_2 and $\Delta\lambda=0.162$ and $\Delta\omega_{\log}=0.2\text{meV}$ for light hydrogenation of Y_2B_2 . These lead to barely changes in T_c for light hydrogenation of the III-TM group. For V-TM group, we also observed a small change in λ and ω_{\log} from non-hydrogenation to light hydrogenation, which is similar to the III-TM group. Therefore, these results in the fact that the non-hydrogenation and light hydrogenation barely become superconductors, except for $\text{V}_2\text{B}_2\text{H}$ which could be superconducting at about 1.3K.

2D materials	λ	ω_{\log} (meV)	ω_2 (meV)	T_c (K) [AD]	T_c (K) [ME]	Refs.
Al ₂ B ₂	0.29	21.05	-	0.10	-	[28]
Mg ₂ B ₂	0.43	42.41	-	3.26	-	[7, 28]
Mo ₂ B ₂	0.40	25.04	-	1.12	-	[28]
W ₂ B ₂	0.38	19.90	-	0.31	-	[28]
Re ₂ B ₂	1.088	6.966	-	5.5	-	[7]
Ti ₂ B ₂	0.31	30.16	-	0.0	-	[29]
Ti ₂ B ₂ H ₄	1.18	47.35	-	48.6	-	[29]
Sc ₂ B ₂	0.19	33.6	-	0.0	-	This work
Y ₂ B ₂	0.23	29.3	-	0.0	-	This work
V ₂ B ₂	0.21	26.6	-	0.0	-	This work
Nb ₂ B ₂	0.23	24.7	-	0.0	-	This work
Sc ₂ B ₂ H	0.26	38.7	-	0.0	-	This work
Y ₂ B ₂ H	0.39	29.5	-	1.3	-	This work
V ₂ B ₂ H	0.27	34.8	-	0.0	-	This work
Nb ₂ B ₂ H	0.32	31.9	-	0.4	-	This work
Sc ₂ B ₂ H ₄	0.68	49.26	-	18.73	46	This work
Y ₂ B ₂ H ₄	0.41	49.52	-	2.74	-	This work
V ₂ B ₂ H ₄	1.29	42.33	58.86	53.35	84	This work
Nb ₂ B ₂ H ₄	1.34	40.88	67.14	54.40	73	This work

Table 5 The table shows the superconducting quantities including the electron-phonon coupling constant λ , the logarithmic average of the phonon energy ω_{\log} , the square average of the phonon energy ω_2 , the critical superconducting temperature T_c [AD] based on the Allen-Dynes formula, and the critical superconducting temperature T_c [ME] based on the closing of the superconducting gap.

For heavy hydrogenation, we still have a low electron-phonon coupling (λ) of 0.68 and 0.41 for Sc₂B₂H₄ and Y₂B₂H₄ even through we have significant increase in ω_{\log} . As a result, the higher λ of Sc₂B₂H₄ leads to a higher $T_c = 18.7\text{K}$, where the lower λ of Y₂B₂H₄ gives $T_c=2.74\text{K}$. However, for the V-TM group, we have significant changes in both λ and ω_{\log} from non-hydrogenation to heavy hydrogenation. The changes are $\Delta\lambda=1.08$ and $\Delta\omega_{\log}=15.73\text{meV}$ for V₂B₂H₄ and $\Delta\lambda=1.11$ and $\Delta\omega_{\log}=16.18\text{meV}$ for Nb₂B₂H₄. Due to these high values of λ in the V-TM group, it leads to a higher T_c for V₂B₂H₄ and Nb₂B₂H₄ compared to the III-TM group. For V₂B₂H₄, it possibly becomes superconducting at least 53.35K up to 84K. Lastly, Nb₂B₂H₄ also shows very promising superconductor of T_c at least 54.40K up to 73K. All the values of T_c , λ , and ω_{\log} are reported in Table 5.

3 Methods.

All calculations of our investigation are based on Density Functional Theory (DFT) implemented in the well-established QUANTUM ESPRESSO (QE) package [32, 33]. The norm-conserving pseudopotentials [34, 35] and the Perdew–Burke–Ernzerhof (GGA-PBE) [36] are used for the exchange-correlation energy functional with wave function and charge density cutoffs of 80 Ry and 320 Ry, respectively. The vacuum thickness was set to be 30Å to make sure no overlap of the wavefunction between monolayers, and the long-range Coulomb interaction was truncated along the z-axis using [37, 38]. The crystal structures were optimized using the BFGS method [39, 40] by fully relaxing the crystal structures with a force threshold of 1.0^{-5} eV/Å. The crystal structure was visualized using VESTA [41] with layered hexagonal transition metal

with $P6/mmm$ space-group symmetry. For electronic structure calculations, we used $24 \times 24 \times 1$ k-point grid for self-consistent calculations to sample the reciprocal space of the Brillouin zone. The electronic density of states and Fermi surfaces were computed using the optimized tetrahedral method for the calculation of non-self-consistency, [42], where the Fermi surface was visualized by XCRYSDEN [43].

To obtain the isotropic Eliashberg spectral function for and M_2B_2 and M_2B_2H , we computed the interatomic force constants (IFC) by performing the Fourier transform of the matrix elements $g_{\mathbf{k}+\mathbf{q},\mathbf{k}}^{q\nu,mn}$ of the coarse $12 \times 12 \times 1$ q-mesh grid calculated by using Density Functional Perturbation Theory (DFPT) [44] implemented in QE. From corrected IFCs, the phonon linewidth, $\gamma_{q\nu}$, was computed,

$$\gamma_{q\nu} = 2\pi\omega_{q\nu} \sum_{nm} \sum_{\mathbf{k}} |g_{\mathbf{k}+\mathbf{q},\mathbf{k}}^{q\nu,mn}|^2 \delta(\epsilon_{\mathbf{k}+\mathbf{q},m} - \epsilon_F) \delta(\epsilon_{\mathbf{k},n} - \epsilon_F) \quad (4)$$

and the electron-phonon coupling, $\lambda_{q\nu}$, associated with the phonon wavevector \mathbf{q} and the phonon mode of μ , as

$$\lambda_{q\nu} = \frac{\gamma_{q\nu}}{\pi N(\epsilon_F) \omega_{q\nu}^2}. \quad (5)$$

The Eliashberg spectral function, $\alpha^2 F(\omega)$, is obtained by

$$\alpha^2 F(\omega) = \frac{1}{2N(\epsilon_F)} \sum_{q\nu} \frac{\gamma_{q\nu}}{\omega_{q\nu}} \delta(\omega - \omega_{q\nu}). \quad (6)$$

To investigate $M_2B_2H_4$, we employ the electron-phonon Wannier-Fourier interpolation method [45–47] within the EPW package [48, 49] to accurately compute the superconducting properties, specifically the electron-phonon coupling (λ) and critical temperature (T_c). This methodology also allows for the detailed analysis of the anisotropic Migdal-Eliashberg theory [50–54] by solving the two coupled nonlinear anisotropic Migdal-Eliashberg equations,

$$Z_{nk}(i\omega_j) = 1 + \frac{\pi T}{N(\epsilon_F)} \sum_{mk'j'} \frac{\omega_{j'}}{\sqrt{\omega_{j'}^2 + \Delta_{mk'}^2(i\omega_{j'})}}, \quad (7)$$

$$Z_{nk}(i\omega_j) \Delta_{mk}(i\omega_j) = \frac{\pi T}{N(\epsilon_F)} \sum_{mk'j'} \frac{\Delta_{mk'}(i\omega_{j'})}{\sqrt{\omega_{j'}^2 + \Delta_{mk'}^2(i\omega_{j'})}} [\lambda(nk, mk', \omega_j - \omega_{j'}) - \mu^*] \delta(\epsilon_{mk'} - \epsilon_F), \quad (8)$$

self-consistently along the imaginary axis at the fermion Matsubara frequencies $\omega_j = (2j + 1)\pi T$. For these calculations, we use the QUANTUM ESPRESSO package with the same computational settings as previously mentioned, followed by Wannier-Fourier interpolation to k- and q-point grids of $120 \times 120 \times 1$ and $60 \times 60 \times 1$, respectively. Employing dense grids ensures the convergence of λ values, as indicated by the stability of the corresponding $\alpha^2 F(\omega)$ and $\lambda(\omega)$ even as the k- and q-point grid densities increase. The Fermi surface thickness was set to 0.55 eV, with a Matsubara frequency cutoff at 1.35 eV. Dirac δ functions were broadened using a Gaussian function with widths of 0.1 eV for electrons and 0.5 meV for phonons when analysing $V_2B_2H_4$, and

$Nb_2B_2H_4$. Due to maximum phonon frequency, the numerical parameters for $Sc_2B_2H_4$, and $Y_2B_2H_4$ were set accordingly. The Fermi surface thickness was set to 0.68 eV, with a Matsubara frequency cutoff at 1.7 eV while we used the same Dirac δ functions for electrons and for phonons. Lastly, the Morel-Anderson pseudopotential was set to $\mu^* = 0.1$ for practical purposes.

The superconducting transition temperature (T_C) was determined using the semi-empirical Allen-Dynes formula [55]:

$$T_c = f_1 f_2 \frac{\omega_{\log}}{1.20} \exp\left(-\frac{1.04(1+\lambda)}{\lambda - \mu^*(1+0.62\lambda)}\right) \quad (9)$$

where the electron-phonon coupling constant λ is derived from the Eliashberg spectral function:

$$\lambda = 2 \int_0^\omega d\Omega \left(\frac{\alpha^2 F(\Omega)}{\Omega}\right), \quad (10)$$

and the logarithmic average phonon frequency is calculated as:

$$\omega_{\log} = \exp\left(\frac{2}{\lambda} \int_0^\infty d\Omega \log(\Omega) \left(\frac{\alpha^2 F(\Omega)}{\Omega}\right)\right). \quad (11)$$

The correction factors f_1 and f_2 are given by:

$$f_1 f_2 = \left(1 + \left(\frac{\lambda}{2.46(1+3.8\mu^*)}\right)\right)^{1/3} \times \left(1 + \frac{\lambda^2 \left(\frac{\omega_2}{\omega_{\log}} - 1\right)}{\lambda^2 + 3.31(1+6.3\mu^*)^2}\right). \quad (12)$$

This $f_1 f_2$ correction factor is applied when the electron-phonon coupling constant λ exceeds 1.0. The mean-square phonon frequency (ω_2) is given by

$$\omega_2 = \sqrt{\frac{2}{\lambda} \int_0^{\omega_{\max}} \alpha^2 F(\omega) \omega d\omega}. \quad (13)$$

4 CONCLUSION.

In this work, we systematically investigate 2D transition metal borides M_2B_2 ($M = Sc, Y, V,$ and Nb) with different levels of hydrogenation. The non-hydrogenation M_2B_2 has been suggested to have dynamical and thermal stability. For M_2B_2 , we again confirm these suggestions with negative formation energies and non-negative phonon dispersion based on DFT computations. For light hydrogenation M_2B_2H and heavy hydrogenation $M_2B_2H_4$, we also found that they are dynamically stable with formation energies even lower than the 2D pristine M_2B_2 . For electronic band structures, we found that the light hydrogenation M_2B_2H can be described as a perturbation of the 2D pristine M_2B_2 . This leads to minor changes in the electronic bands and in the electronic density of states. A major modification of the electronic bands occurs when applying heavy hydrogenation $M_2B_2H_4$. This results in many changes from

M_2B_2 and M_2B_2H to $M_2B_2H_4$. As a result, these results suggest that the disrupted evolution of the electronic band topology of Fermi surfaces can be slightly changed and heavily disrupted because of the amount of hydrogenation. For the III-TM group (Sc, Y), we found that EDOS decreases significantly at the Fermi level. The reduction in EDOS occurs due to the decrease of d-orbital electrons as a result of the bonding of additional hydrogen atoms, especially for $Y_2B_2H_4$ in which the d-orbital electrons no longer completely dominate at the Fermi level. On the other hand, the V-TM group (Sc, Y) shows a higher EDOS compared to the III-TM group, and even higher for $V_2B_2H_4$ because of a significant van Hove singularity located almost at the Fermi level. This would favor λ for the heavy hydrogenation of the V-TM group rather than the heavy hydrogenation of the III-TM group. For phonons, the phonon dispersion of light hydrogenation is similar to that of non-hydrogenation, with three additional optical modes of hydrogen atom dominating the highest phonon spectrum. For the heavy hydrogenation $M_2B_2H_4$, the phonon dispersion is completely disturbed, and the new phonon spectrum eventually leads to new superconducting properties. Even through, ω_{log} is higher for the heavy hydrogenation of the III-TM group than that of the V-TM group, λ is higher for the heavy hydrogenation of V-TM group than that of III-TM group. As a result, $Nb_2B_2H_4$ shows the most promising superconductor with T_c of at least 40.1K where T_c of $V_2B_2H_4$, $Sc_2B_2H_4$, and $Y_2B_2H_4$ are at least 33.4, 18.3, and 4.3K, respectively.

Acknowledgments. This research project is supported by the Second Century Fund (C2F), Chulalongkorn University. The authors acknowledge the National Science and Technology Development Agency, National e-Science Infrastructure Consortium, Chulalongkorn University and the Chulalongkorn Academic Advancement into Its 2nd Century Project (Thailand) for providing computing infrastructure that has contributed to the research results reported within this paper. URL:www.e-science.in.th. GJA acknowledges funding from the ERC project Hecate. The authors acknowledge NSTDA Supercomputer Center (ThaiSC) for providing LANTA computing resources for this work. This also work used the Cirrus UK National Tier-2 HPC Service at EPCC (<http://www.cirrus.ac.uk>) funded by the University of Edinburgh and EPSRC (EP/P020267/1).

References

- [1] Nagamatsu, J., Nakagawa, N., Muranaka, T., Zenitani, Y., Akimitsu, J.: Superconductivity at 39 k in magnesium diboride. *nature* **410**(6824), 63–64 (2001)
- [2] Bardeen, J., Cooper, L.N., Schrieffer, J.R.: Microscopic theory of superconductivity. *Physical Review* **106**(1), 162 (1957)
- [3] Leyarovska, L., Leyarovski, E.: A search for superconductivity below 1 k in transition metal borides. *Journal of the Less Common Metals* **67**(1), 249–255 (1979)
- [4] Gasparov, V.A., Sidorov, N., Zver'kova, I.I., Kulakov, M.: Electron transport in diborides: observation of superconductivity in zrb 2. *Journal of Experimental and*

Theoretical Physics Letters **73**, 532–535 (2001)

- [5] Rosner, H., Pickett, W., Drechsler, S.-L., Handstein, A., Behr, G., Fuchs, G., Nenkov, K., Müller, K.-H., Eschrig, H.: Electronic structure and weak electron-phonon coupling in tab 2. *Physical Review B* **64**(14), 144516 (2001)
- [6] Cheng, S.-H., Zhang, Y., Wang, H.-Z., Li, Y.-L., Yang, C., Wang, Y.: Fabrication and characterization of superconducting mgb2 thin film on graphene. *AIP Advances* **8**(7) (2018)
- [7] Sevik, C., Bekaert, J., Petrov, M., Milošević, M.V.: High-temperature multigap superconductivity in two-dimensional metal borides. *Physical Review Materials* **6**(2), 024803 (2022)
- [8] Ashcroft, N.: Hydrogen dominant metallic alloys: high temperature superconductors? *Physical Review Letters* **92**(18), 187002 (2004)
- [9] McMahan, J.M., Ceperley, D.M.: High-temperature superconductivity in atomic metallic hydrogen. *Physical Review B* **84**(14), 144515 (2011)
- [10] Duan, D., Liu, Y., Tian, F., Li, D., Huang, X., Zhao, Z., Yu, H., Liu, B., Tian, W., Cui, T.: Pressure-induced metallization of dense (h2s) 2h2 with high-t c superconductivity. *Scientific reports* **4**(1), 6968 (2014)
- [11] Peng, F., Sun, Y., Pickard, C.J., Needs, R.J., Wu, Q., Ma, Y.: Hydrogen clathrate structures in rare earth hydrides at high pressures: possible route to room-temperature superconductivity. *Physical review letters* **119**(10), 107001 (2017)
- [12] Liu, H., Naumov, I.I., Hoffmann, R., Ashcroft, N., Hemley, R.J.: Potential high-*t_c* superconducting lanthanum and yttrium hydrides at high pressure. *Proceedings of the National Academy of Sciences* **114**(27), 6990–6995 (2017)
- [13] Drozdov, A., Eremets, M., Troyan, I., Ksenofontov, V., Shylin, S.I.: Conventional superconductivity at 203 kelvin at high pressures in the sulfur hydride system. *Nature* **525**(7567), 73–76 (2015)
- [14] Einaga, M., Sakata, M., Ishikawa, T., Shimizu, K., Eremets, M.I., Drozdov, A.P., Troyan, I.A., Hirao, N., Ohishi, Y.: Crystal structure of the superconducting phase of sulfur hydride. *Nature physics* **12**(9), 835–838 (2016)
- [15] Drozdov, A., Kong, P., Minkov, V., Besedin, S., Kuzovnikov, M., Mozaffari, S., Balicas, L., Balakirev, F., Graf, D., Prakapenka, V., *et al.*: Superconductivity at 250 k in lanthanum hydride under high pressures. *Nature* **569**(7757), 528–531 (2019)
- [16] Somayazulu, M., Ahart, M., Mishra, A.K., Geballe, Z.M., Baldini, M., Meng, Y.,

- Struzhkin, V.V., Hemley, R.J.: Evidence for superconductivity above 260 k in lanthanum superhydride at megabar pressures. *Physical review letters* **122**(2), 027001 (2019)
- [17] Liu, X., Zhang, L., Wang, M., Huang, X., Liu, L., Jia, Y.: Realizing high- T_c ambient-pressure superconductivity in hole-doped hydride mg (bh4) 2. *Materials Today Physics* **40**, 101299 (2024)
- [18] Seeyangnok, J., Ul Hassan, M.M., Pinsook, U., Ackland, G.: Superconductivity and electron self-energy in tungsten-sulfur-hydride monolayer. *2D Materials* **11**(2), 025020 (2024)
- [19] Ul Hassan, M.M., Pinsook, U.: Superconductivity in monolayer janus titanium-sulfurhydride (tish) at ambient pressure. *Journal of Physics: Condensed Matter* (2024)
- [20] Li, J., Wei, L., Shi, X., Shi, L., Si, J., Liu, P.-F., Wang, B.-T.: Machine learning accelerated discovery of superconducting two-dimensional janus transition metal sulfhydrates. *Physical Review B* **109**(17), 174516 (2024)
- [21] Ku, R., Yan, L., Si, J.-G., Zhu, S., Wang, B.-T., Wei, Y., Pang, K., Li, W., Zhou, L.: Ab initio investigation of charge density wave and superconductivity in two-dimensional janus 2 h/1 t-mosh monolayers. *Physical Review B* **107**(6), 064508 (2023)
- [22] Liu, P.-F., Zheng, F., Li, J., Si, J.-G., Wei, L., Zhang, J., Wang, B.-T.: Two-gap superconductivity in a janus mosh monolayer. *Physical Review B* **105**(24), 245420 (2022)
- [23] Savini, G., Ferrari, A., Giustino, F.: First-principles prediction of doped graphane as a high-temperature electron-phonon superconductor. *Physical review letters* **105**(3), 037002 (2010)
- [24] Jiao, N., Liu, H.-D., Yang, L., Li, Y.-P., Zheng, M., Lu, H.-Y., Zhang, P.: Hydrogenation-induced high-temperature superconductivity in two-dimensional molybdenum carbide mo2c3. *Europhysics Letters* **138**(4), 46002 (2022)
- [25] Yan, X., Ding, S., Zhang, X., Bergara, A., Liu, Y., Wang, Y., Zhou, X.-F., Yang, G.: Enhanced superconductivity in cuh 2 monolayers. *Physical Review B* **106**(1), 014514 (2022)
- [26] Bekaert, J., Petrov, M., Aperis, A., Oppeneer, P.M., Milošević, M.: Hydrogen-induced high-temperature superconductivity in two-dimensional materials: The example of hydrogenated monolayer mgb 2. *Physical review letters* **123**(7), 077001 (2019)
- [27] Li, Y.-P., Yang, L., Liu, H.-D., Jiao, N., Ni, M.-Y., Hao, N., Lu, H.-Y., Zhang,

- P.: Phonon-mediated superconductivity in two-dimensional hydrogenated phosphorus carbide: Hpc 3. *Physical Chemistry Chemical Physics* **24**(16), 9256–9262 (2022)
- [28] Han, Y.-L., Liu, H.-D., Jiao, N., Zheng, M.-M., Lu, H.-Y., Wang, B.-T., Zhang, P.: Theoretical prediction of superconductivity in two-dimensional hydrogenated metal diboride: M_2B_2H ($M = Al, Mg, Mo, W$). *Physical Review Materials* **7**(11), 114802 (2023)
- [29] Han, Y.-L., Li, Y.-P., Yang, L., Liu, H.-D., Jiao, N., Wang, B.-T., Lu, H.-Y., Zhang, P.: High-temperature superconductivity in two-dimensional hydrogenated titanium diboride: $Ti_2B_2H_4$. *Materials Today Physics* **30**, 100954 (2023)
- [30] Bo, T., Liu, P.-F., Xu, J., Zhang, J., Chen, Y., Eriksson, O., Wang, F., Wang, B.-T.: Hexagonal Ti_2B_2 monolayer: a promising anode material offering high rate capability for li-ion and na-ion batteries. *Physical Chemistry Chemical Physics* **20**(34), 22168–22178 (2018)
- [31] He, Q., Li, Z., Xiao, W., Zhang, C., Zhao, Y.: Computational investigation of 2d 3d/4d hexagonal transition metal borides for metal-ion batteries. *Electrochimica Acta* **384**, 138404 (2021)
- [32] Giannozzi, P., Baroni, S., Bonini, N., Calandra, M., Car, R., Cavazzoni, C., Ceresoli, D., Chiarotti, G.L., Cococcioni, M., Dabo, I., *et al.*: Quantum espresso: a modular and open-source software project for quantum simulations of materials. *Journal of physics: Condensed matter* **21**(39), 395502 (2009)
- [33] Giannozzi, P., Andreussi, O., Brumme, T., Bunau, O., Nardelli, M.B., Calandra, M., Car, R., Cavazzoni, C., Ceresoli, D., Cococcioni, M., *et al.*: Advanced capabilities for materials modelling with quantum espresso. *Journal of physics: Condensed matter* **29**(46), 465901 (2017)
- [34] Hamann, D.: Optimized norm-conserving vanderbilt pseudopotentials. *Physical Review B* **88**(8), 085117 (2013)
- [35] Schlipf, M., Gygi, F.: Optimization algorithm for the generation of oncv pseudopotentials. *Computer Physics Communications* **196**, 36–44 (2015)
- [36] Perdew, J.P., Burke, K., Ernzerhof, M.: Generalized gradient approximation made simple. *Physical review letters* **77**(18), 3865 (1996)
- [37] Sohier, T., Calandra, M., Mauri, F.: Density functional perturbation theory for gated two-dimensional heterostructures: Theoretical developments and application to flexural phonons in graphene. *Physical Review B* **96**(7), 075448 (2017)
- [38] Sohier, T., Gibertini, M., Calandra, M., Mauri, F., Marzari, N.: Breakdown of

- optical phonons' splitting in two-dimensional materials. *Nano letters* **17**(6), 3758–3763 (2017)
- [39] Pfrommer, B.G., Cote, M., Louie, S.G., Cohen, M.L.: Relaxation of crystals with the quasi-Newton method. *J. Comput. Phys.* **131**, 233–240 (1997)
- [40] Liu, D.C., Nocedal, J.: On the limited memory bfgs method for large scale optimization. *Mathematical programming* **45**(1-3), 503–528 (1989)
- [41] Momma, K., Izumi, F.: Vesta 3 for three-dimensional visualization of crystal, volumetric and morphology data. *Journal of applied crystallography* **44**(6), 1272–1276 (2011)
- [42] Kawamura, M., Gohda, Y., Tsuneyuki, S.: Improved tetrahedron method for the brillouin-zone integration applicable to response functions. *Physical Review B* **89**(9), 094515 (2014)
- [43] Kokalj, A.: Computer graphics and graphical user interfaces as tools in simulations of matter at the atomic scale. *Computational Materials Science* **28**(2), 155–168 (2003)
- [44] Baroni, S., De Gironcoli, S., Dal Corso, A., Giannozzi, P.: Phonons and related crystal properties from density-functional perturbation theory. *Reviews of modern Physics* **73**(2), 515 (2001)
- [45] Qiao, J., Pizzi, G., Marzari, N.: Automated mixing of maximally localized wannier functions into target manifolds. *npj Computational Materials* **9**(1), 206 (2023)
- [46] Giustino, F.: Electron-phonon interactions from first principles. *Reviews of Modern Physics* **89**(1), 015003 (2017)
- [47] Giustino, F., Cohen, M.L., Louie, S.G.: Electron-phonon interaction using wannier functions. *Physical Review B* **76**(16), 165108 (2007)
- [48] Noffsinger, J., Giustino, F., Malone, B.D., Park, C.-H., Louie, S.G., Cohen, M.L.: Epw: A program for calculating the electron–phonon coupling using maximally localized wannier functions. *Computer Physics Communications* **181**(12), 2140–2148 (2010)
- [49] Poncé, S., Margine, E.R., Verdi, C., Giustino, F.: Epw: Electron–phonon coupling, transport and superconducting properties using maximally localized wannier functions. *Computer Physics Communications* **209**, 116–133 (2016)
- [50] Fröhlich, H.: Theory of the superconducting state. i. the ground state at the absolute zero of temperature. *Physical Review* **79**(5), 845 (1950)
- [51] Migdal, A.: Interaction between electrons and lattice vibrations in a normal metal. *Sov. Phys. JETP* **7**(6), 996–1001 (1958)

- [52] Eliashberg, G.: Interactions between electrons and lattice vibrations in a superconductor. *Sov. Phys. JETP* **11**(3), 696–702 (1960)
- [53] Nambu, Y.: Quasi-particles and gauge invariance in the theory of superconductivity. *Physical Review* **117**(3), 648 (1960)
- [54] Margine, E.R., Giustino, F.: Anisotropic migdal-eliashberg theory using wannier functions. *Physical Review B* **87**(2), 024505 (2013)
- [55] Allen, P.B., Dynes, R.: Transition temperature of strong-coupled superconductors reanalyzed. *Physical Review B* **12**(3), 905 (1975)

COMPETING INTERESTS

The authors declare no competing financial or non-financial interests.

DATA AVAILABILITY

Data will be available from the authors on request.

AUTHOR CONTRIBUTIONS

Jakkapat Seeyangnok performed structural, electronic, phonon and superconductivity calculations, analysed the results, and wrote the first draft manuscript. Udomsilp Pinsook coordinated the project, analysed the results, and wrote the manuscript. Graeme Ackland analysed the results, supervised the project, and wrote the final manuscript. All authors have approved the final manuscript.